Chemosphere 288 (2022) 132494

Contents lists available at ScienceDirect

Chemosphere

journal homepage: www.elsevier.com/locate/chemosphere

Efficient antibiotics removal via the synergistic effect of manganese ferrite and MoS_2

Huan Yi [a,b,c,1], Cui Lai [b,c,1], Eydhah Almatrafi [c,1], Xiuqin Huo [b], Lei Qin [b], Yukui Fu [b], Chengyun Zhou [a,b,c], Zhuotong Zeng [a,b,c,**], Guangming Zeng [a,b,c,*]

[a] Department of Dermatology, Second Xiangya Hospital, Central South University, Changsha, 410011, PR China
[b] College of Environmental Science and Engineering and Key Laboratory of Environmental Biology and Pollution Control (Ministry of Education), Hunan University, Changsha, Hunan, 410082, PR China
[c] Center of Research Excellence in Renewable Energy and Power Systems, Center of Excellence in Desalination Technology, Department of Mechanical Engineering, Faculty of Engineering-Rabigh, King Abdulaziz University, Jeddah, 21589, Saudi Arabia

HIGHLIGHTS

- Green photo-Fenton process is a potential method for antibiotics pollution treatment.
- Stable manganese ferrite $MnFe_2O_4$-MoS_2 (FMG) composites were synthesized.
- FMG composites show good performance on tetracycline degradation.
- h^+, •OH and $^1O_2$ participate in TC photodegradation, and h^+ plays a key role.
- OH has a great impact on the mineralization ability of this photo-Fenton process.

GRAPHICAL ABSTRACT

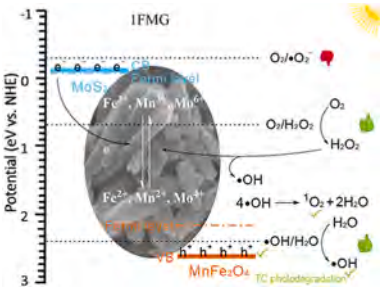

ARTICLE INFO

Handling Editor: Jun Huang

Keywords:
Antibiotics removal
Photo-Fenton
$MnFe_2O_4$
MoS_2
Easy recycle

ABSTRACT

The use of antibiotics for beings is a most significant milestone in present era. However, owing to the excessive use, a large amount of antibiotics accumulated in water, leading to serious pollution. An efficient method is urgently needed to treat the antibiotics pollution. Photo-Fenton process is a green method with utilizing solar energy. Catalyst is important. This work combines manganese ferrite $MnFe_2O_4$ and MoS_2 to synthesize $MnFe_2O_4$-MoS_2 (FMG) composite as the catalyst of photo-Fenton process, which shows good performance on tetracycline antibiotics degradation. Light intensity exhibits positive correlation with the catalytic activity. h^+, •OH and $^1O_2$ participate in tetracycline degradation. h^+ plays a key role in tetracycline removal. •OH has a little impact on tetracycline removal, but it has a great impact on the mineralization ability of this photo-Fenton process. Additionally, cycling experiments confirm the stability of FMG. And owing to its magnetism, FMG can be easily recycled by external magnetic field. This photo-Fenton process over FMG with utilizing the synergism of $MnFe_2O_4$ and MoS_2 is a promising method for antibiotics pollution treatment.

* Corresponding author. College of Environmental Science and Engineering and Key Laboratory of Environmental Biology and Pollution Control (Ministry of Education), Hunan University, Changsha, Hunan, 410082, PR China.
** Corresponding author. Department of Dermatology, Second Xiangya Hospital, Central South University, Changsha, 410011, PR China.
E-mail addresses: zengzhuotong@csu.edu.cn (Z. Zeng), zgming@hnu.edu.cn (G. Zeng).
[1] These authors contribute equally to this article.

https://doi.org/10.1016/j.chemosphere.2021.132494
Received 4 July 2021; Received in revised form 29 September 2021; Accepted 5 October 2021
Available online 7 October 2021

1. Introduction

Antibiotics have been widely used as antibacterial agents in treating disease for beings (Yu et al., 2021b). High influent concentration, like 1616 ng L^{-1} of tetracycline (TC), was detected in municipal sewage treatment plant (Shao and Wu, 2020). This lead to a serious pollution, and antibiotics would increase chemical oxygen demand and negatively affect the microbial community structure in water (Yi et al., 2019; Stokes et al., 2020; Yu et al., 2021c). Notably, antibiotic pollution is happening directly to humans. According to global ICU infection data, drug resistance caused by overuse of antibiotics will lead to an estimated 10 million deaths a year in 2050 (O'Neill, 2016). Treatment for antibiotics is urgently needed. However, owing to the stubborn ring structure and the developed bacterial resistance, using common wastewater treatment technologies (e.g. adsorption, membrane separation, and biological treatment) cannot remove TC efficiently (Fu et al., 2020; Li et al., 2020a; Yu et al., 2021a).

Photocatalytic process has been proved to be a good solution for TC removal (Yi et al., 2018; Li et al., 2020b; Yang et al., 2020). Owing to the hard sedimentation and centrifugation process at industrial scale, fabricating a magnetic composite catalyst that can be easily recycled via magnetic separation. Spine ferrite is an ideal material with showing soft

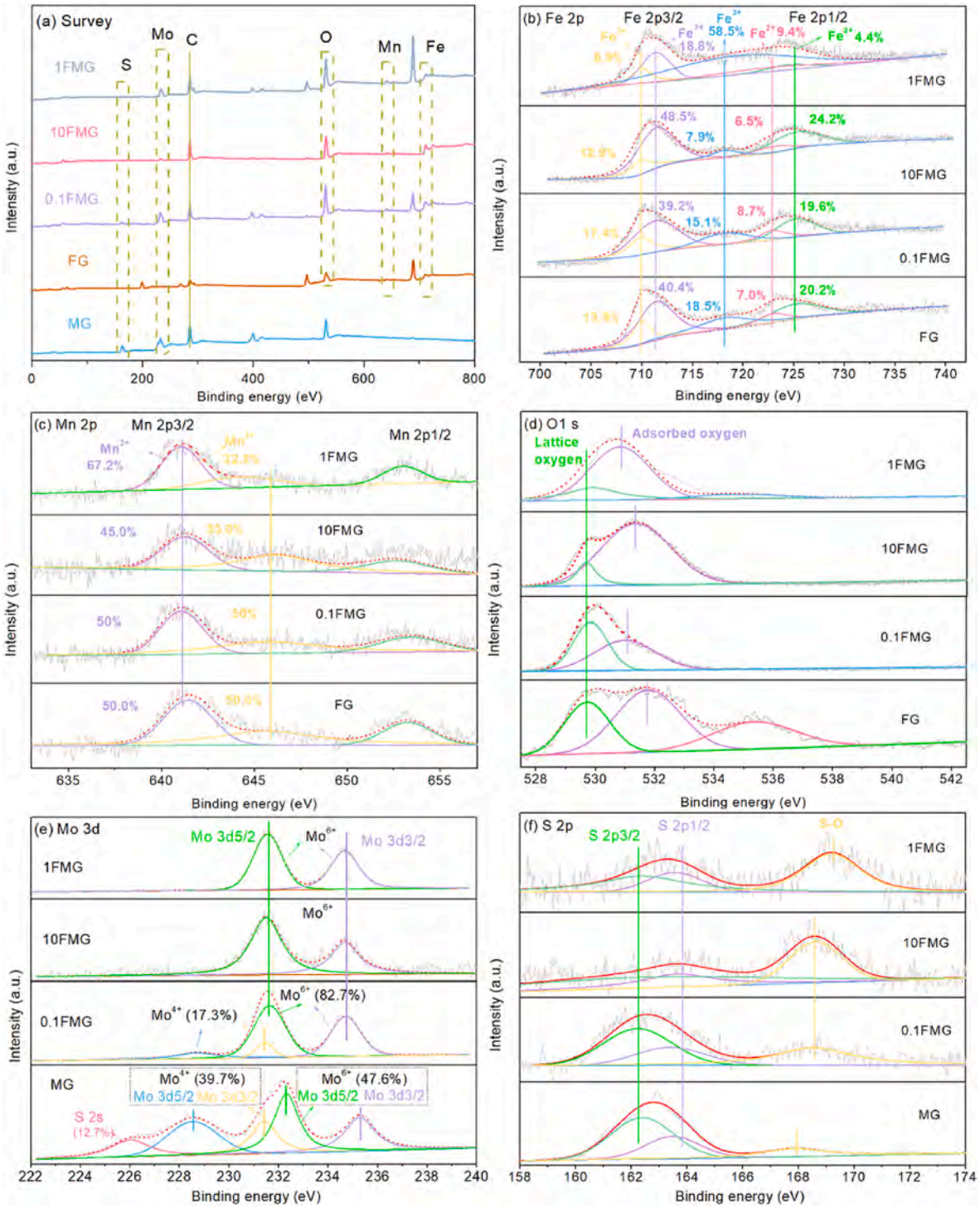

Fig. 1. XPS analysis of the samples: (a) survey spectra, (b) Fe 2p, (c) Mn 2p, (d) O 1s, (e) Mo 3d, (f) S 2p.

magnetic property and high catalytic activity, like $ZnFe_2O_4$ for photo induced PMS activation (Zhong et al., 2021). $MnFe_2O_4$ is a popular cubic spine ferrite with functional surface, showing high adsorption ability (Hou et al., 2021; Gautam et al., 2017; Wang et al., 2020). And it exhibits good biocompatibility. However, photocatalytic system based on $MnFe_2O_4$ is not efficient. Molybdenum disulfide (MoS_2), a common used photocatalyst, has large surface area and suitable band gap for visible-light absorption (Pang et al., 2019). But, the photocatalytic process over MoS_2 cannot generate enough radicals to degrade TC owing to the low valence band (VB) edge potential, and it is difficult to recycle MoS_2 from this process (Samakchi et al., 2018; Liu et al., 2019). Combining $MnFe_2O_4$ and MoS_2 shows the potential to solve these drawbacks simultaneously. Apart from being the main component of catalyst, MoS_2 can act as co-catalyst to accelerate the Mn^{2+}/Mn^{3+} and Fe^{2+}/Fe^{3+} cycle to improve the catalytic efficiency.

This work reports the photo-Fenton process catalyzed by $MnFe_2O_4$/MoS_2 (FM) composites. Mo, Mn and Fe with variable valence benefit the transfer of electrons in the process to improve the oxidation efficiency. The stable and recyclable catalytic performance of FM is tested. The effects of different catalysts, TC concentration and light intensity on the performance of TC degradation are studied. The intermediate products are detected and the degradation pathways are discussed to better know the process action. The role of radicals generated in the process and mechanism are also investigated. Overall, this photo-Fenton process over FM exhibits potential practical utility for aqueous organic pollutants treatment.

2. Experimental

2.1. Synthesis of catalysts

All the reagents are analytical grade. Deionized water was used in the experiment, and the resistivity was 18.2 MΩ cm (Milli-Q Millipore). The composite FM synthesized via a solvothermal process with ethylene glycol as the solution is marked as FMG, including four steps: (i) $MnCl_2{\cdot}4H_2O$ and $FeCl_3{\cdot}6H_2O$ (with 1 : 2 in mol) are dissolved in 20 mL ethylene glycol, then adding 7.2 g sodium acetate (NaAc) and 2.0 g polyethylene glycol to obtain solution A after 60 min stirring; (ii) $(NH_4)_6Mo_7O_{24}{\cdot}4H_2O$ and thiourea (1 : 40 in mol) are dissolved in 20 mL ethylene glycol to obtain solution B after 30 min ultrasonication; (iii) adding A to B under stirring to get mixture solution; (iv) transfer to Teflon-lined autoclave, heat to 180 °C and maintain for 22 h (Shen et al., 2015). The mixture with mol ratio of Mn (in A): Mo (in B) located at 1: 1, 10: 1 and 1: 10 are obtained to synthesize various composites and marked as 1FMG, 10FMG, 0.1FMG, respectively. Parallel synthesis process without step (ii) and (iii) was used to obtain pure $MnFe_2O_4$ (FG). MoS_2 (MG) was prepared through the parallel synthesis process without step (i) and (iii).

2.2. Characterization of catalysts

X-ray photoelectron spectroscopy (XPS, Thermo Scientific K-Alpha+) is used to investigate the surface elemental compositions. Scanning electron microscopy (SEM, SIGMA HD), transmission electron microscopy (TEM) and high resolution TEM (TEM, JEOL JEM 2100) are employed to show the information of morphology and crystal lattice. The specific surface area and pore size are recorded by Brunauer-Emmett-Teller (BET, ASAP, 2020 Plus HD88). UV–vis diffuse reflectance spectrophotometer (DRS, Hitachi U4100 UV), Mott-Schottky (M − S) analysis, and linear sweep voltammetry (LSV) are employed to study the optical properties.

2.3. Photo-Fenton experiments

All the water samples are filtrated by 0.45 μm filter membrane. TC is added to water to obtain 10 mg/L solution. 20 mg catalyst is added to 100 mL TC solution. Dark reaction is performed firstly to reach the adsorption/desorption equilibrium. Then, the solution is irradiated with Xe lamp (>420 nm, CELHXF300) for 1 h. Reaction solution is collected at given time interval and then filtered through 0.45 μm membrane filters. The concentration of TC is analyzed via Shimadzu UV–vis spectrophotometer (characteristic band at 357 nm). TC intermediate products are determined by high-performance liquid chromatography-mass spectrometry (HPLC-MS, 1290/6460 Triple Quad). The test method of HPLC-MS is same as that in our previous work (Yang et al., 2018). Mineralization of TC solution was analyzed by testing the total organic carbon (TOC) on Analytik Jena AG (Multi N/C 2100).

2.4. Detection of generated radicals

Trapping tests are used to explore the role of these active species (i.e., h^+, $\bullet O_2^-$, $^1O_2$ and •OH) in TC degradation. Tetramethylpiperidine (TEMPOL), Isopropanol (IPA), Ethylenediamine tetraacetic acid disodium salt (EDTA-2Na), and L-tryptophan (LTP) are used as the scavengers for $\bullet O_2^-$, •OH, h^+, and $^1O_2$, respectively. LC-MS is also used to detect the intermediates generated in the TC photodegradation process with adding the scavengers.

3. Results and discussion

3.1. Characterizations

3.1.1. Surface element analysis

Surface elemental compositions of the samples are analyzed by XPS. Fig. 1a shows the full-scale spectrum. Binding energy (BE) of Fe 2p, Mn 2p, O 1s, Mo 3d and S 2p are detected in 1FMG, 10FMG and 0.1FMG composites. Fe, Mn and O exist in FG. However, beside Mo and S, O also exist in MG, possibly ascribed to the oxygen of adsorbed –OH form ethylene glycol or H_2O molecules from air.

Fig. 1b is the high resolution spectrum of Fe 2p. It can observe two obvious peaks at ~724 eV and ~711 eV that are respectively belonged to the BE of Fe $2p_{1/2}$ and Fe $2p_{3/2}$, and a satellite peak at 718.2 eV is ascribed to the presence of Fe^{3+}. Moreover, both Fe^{3+} and Fe^{2+} existed in Fe $2p_{1/2}$ and Fe $2p_{3/2}$. The BE at 709.9 eV and 711.4 eV belonged to Fe^{3+} and Fe^{2+} of Fe $2p_{3/2}$, while 722.9 eV and 725.2 eV BE belong to Fe^{3+} and Fe^{2+} of Fe $2p_{1/2}$ (Zhao et al., 2020). Based on the peak area, the content of Fe^{3+} and Fe^{2+} can be obtained, which is different in composites and FG. The ratio of Fe^{2+} in 0.1FMG is nearest to that in FG. This reveals that reactions happened between $MnFe_2O_4$ and MoS_2. Since Fe^{3+} and Fe^{2+} co-existed in FMG and FG, it is reasonable to believe the presence of Mn^{3+} and Mn^{2+}.

In the Mn 2p spectrum (Fig. 1c), the binding energy of Mn^{3+} (645.8 eV) and Mn^{2+} (641.3 eV) can be divided from Mn $2p_{3/2}$ peak. The content of $Mn^{3+}$and Mn^{2+} in the prepared samples is also not the same, and the ratio of $Mn^{3+}$and Mn^{2+} in 0.1FMG is closest to FG, which is consistent with the findings in Fe 2p spectrum. Mn^{3+} can better capture holes to improve catalytic performance (Chen et al., 2014). Moreover, Mn 2p1/2 (652.5 eV) is observed.

High resolution spectrum of O 1s is shown in Fig. 1d. BE at 529.7 eV is ascribed to lattice oxygen, while BE at ~531 eV (530.9 eV in 1FMG, 531.4 eV in 10FMG, 531.1 eV in 0.1FMG and 531.7 eV in FG) might be owing to the adsorbed oxygen from –OH, H_2O or air. Additionally, the satellite peak of FG at 531.5 eV confirms the presence of lattice oxygen Mn-O.

Mo 3d spectrum is shown in Fig. 1e. The peak appeared at 226.0 eV belongs to the BE of S 2s. Mo $3d_{5/2}$ and $3d_{3/}2$ peak with Mo^{6+} are observed in all the samples. In 0.1FMG and FG, Mo^{4+} can be divided from Mo $3d_{5/2}$. However, the content of Mo^{4+} divided from $3d_{5/2}$ is lower than Mo^{6+}. It suggests that Mo is oxidized in the reaction, leading to the generation of MoO_x (x = 2 or 3), which can also provide active sites (Vesel et al., 2018). This can explain the low signal of MoS_2 in XRD.

S-O is found in S 2p spectrum (the rightmost peak in Fig. 1f) (Chen

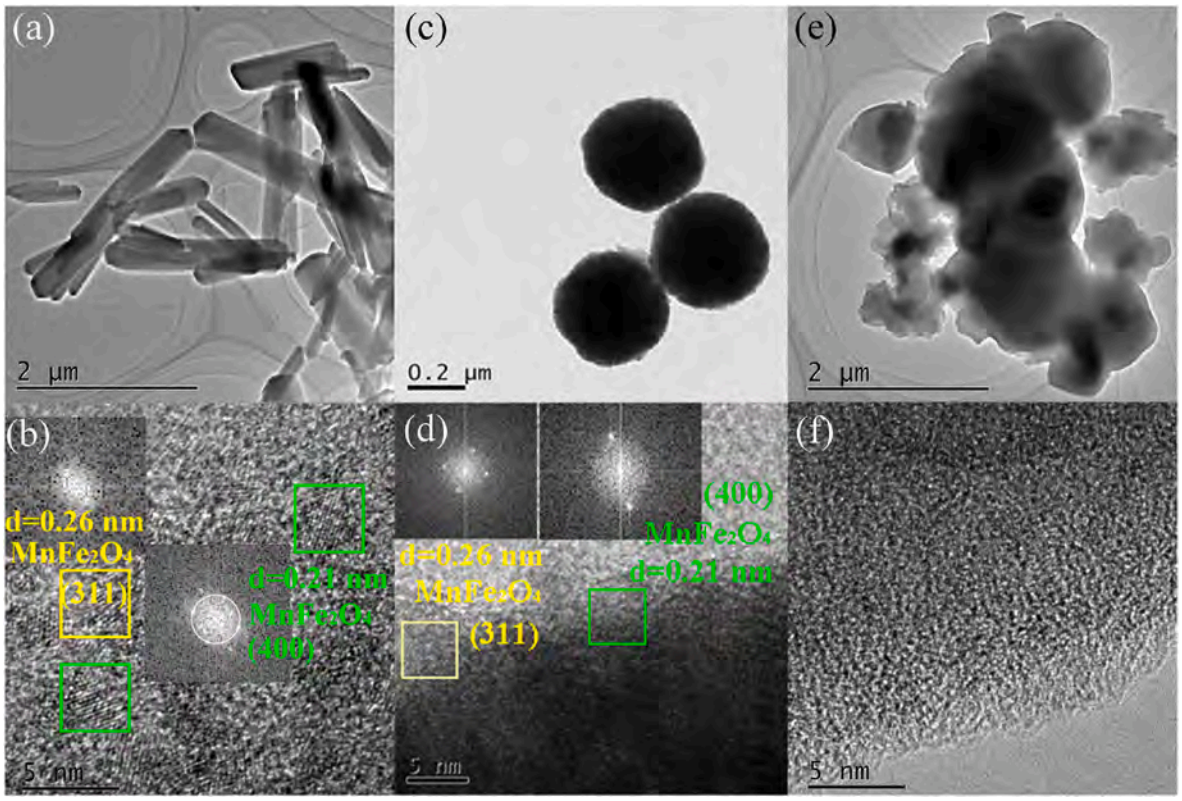

Fig. 2. TEM and HR-TEM images of (a, b) 1FMG, (c, d) 10FMG, and (e, f) 0.1FMG.

et al., 2020). Corresponding to Mo, the least oxidation of S occurs in MG, and the next is 0.1FMG. S $2p_{3/2}$ (162.4 eV) and $2p_{1/2}$ (163.6 eV) peaks are found. The spin-orbit energy separation of 1.2 eV is consistent with MoS_2. Besides, XPS valence spectra of FG and MG are measured to obtain the VB. As shown in Fig. S1, the VB value of FG and MG is 2.94 V and 0.12 V, respectively.

3.1.2. Morphology

Morphology and microstructure of samples are performed by SEM and TEM. SEM images are presented in Fig. S2. FG show spherical shape with pores. MG also exhibits spherical shape, but the surface is smooth. Both the size of FG and MG is not uniform. Morphologies of 1FMG, 10FMG and 0.1FMG are also observed in TEM images (Fig. 2), which are consistent with SEM. As can be seen from Fig. 1a, 1FMG exhibits stick-like shape with the size at ~2 × 0.3 μm. These sticks are well dispersed and not accumulated. The corresponding HRTEM images show two lattice fringes with lattice spacing at 0.21 nm and 0.26 nm, belonging to (400) and (311) plane of $MnFe_2O_4$, respectively. It can be observed that 10FMG shows regular spherical shape with a diameter at ~0.4 μm. Three kinds of lattice spacing and crystal planes are observed

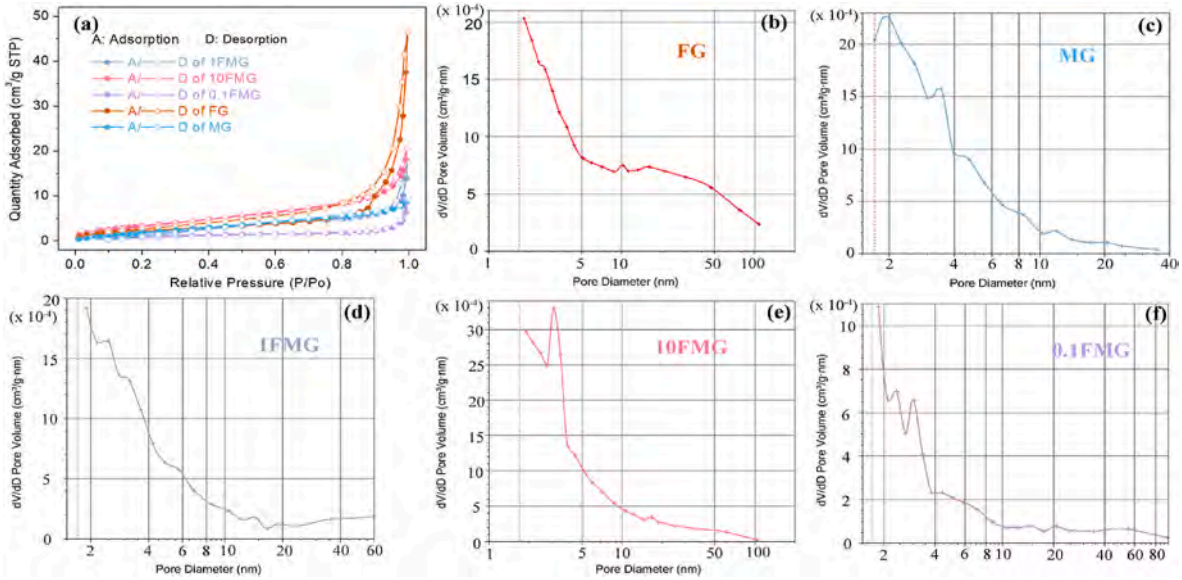

Fig. 3. N_2 adsorption-desorption isotherm of all the samples (a), and pore diameter distribution of FG (b), MG (c), 1FMG (d), 10FMG (e), 0.1FMG (f).

Table 1
BET surface, average pore volume and average pore diameter of the prepared samples.

Samples	1FMG	10FMG	0.1FMG	FG	MG
BET surface (m^2/g)	9.03	13.62	4.34	8.78	9.93
Total pore volume (cm^3/g)	0.027	0.032	0.135	0.070	0.014
Average pore diameter (nm)	9.05	8.75	14.99	17.76	4.60

in HRTEM images, including 0.21 nm (400), 0.26 nm (311) and 0.30 nm (220) (Zhang et al., 2014; Wang et al., 2017). All of them are the crystal planes of $MnFe_2O_4$. No MoS_2 crystal plane is observed in the HRTEM images of 1FMG and 10FMG. There are two possible reasons: i) the content of MoS_2 is low, ii) MoS_2 is surrounded by $MnFe_2O_4$. Therefore, only $MnFe_2O_4$ lattice can be observed from the surface. The shape of 0.1FMG performed in Fig. 2c is spherical but not regular with multiple sizes. No crystal lattice was magnified by HRTEM, indicating the formation of amorphous substance. It is speculated that amorphous MoS_2 is formed outside the $MnFe_2O_4$ in 0.1FMG.

3.1.3. Surface area and pore size

The surface area and pore distribution of these prepared samples are explored via nitrogen adsorption-desorption isotherms experiments. As can be seen in Fig. 3a, the basic shape of N_2 adsorption-desorption isotherm of all the samples are typical IV type, indicating the presence of mesoporous. Moreover, the samples possess H3-type hysteric ring that suggest the slit structures. The BET surface area in descending order is: 10FMG > MG > 1FMG > FG > 0.1FMG (Table 1). The pore diameter distributions are shown in Fig. 3b–f. Pores of FG and 10FMG range from 1 nm to 100 nm. 0.1 FMG pores are in the range of 0–90 nm. 1FMG Pores range from 0 nm to 60 nm. MG shows the least range of pore diameter (0–40 nm), corresponding to the least average pore diameter (4.6 nm). The BET specific surface area and pore size of different catalysts are different. The specific surface area of the catalyst can explain the exposure of the surface active site. The contact between the active site and the target contaminant is also affected by the structure of the catalyst.

3.1.4. Optical property

Related optical properties of the prepared samples are explored by

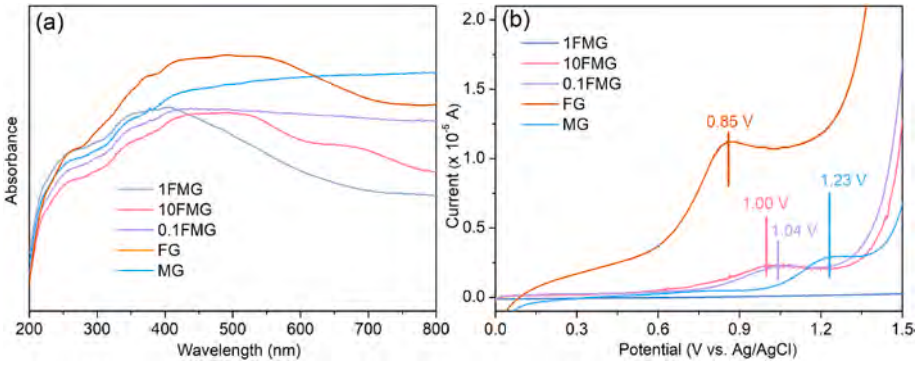

Fig. 4. (a) UV–Vis absorption spectra and (b) LSV curve of the prepared samples.

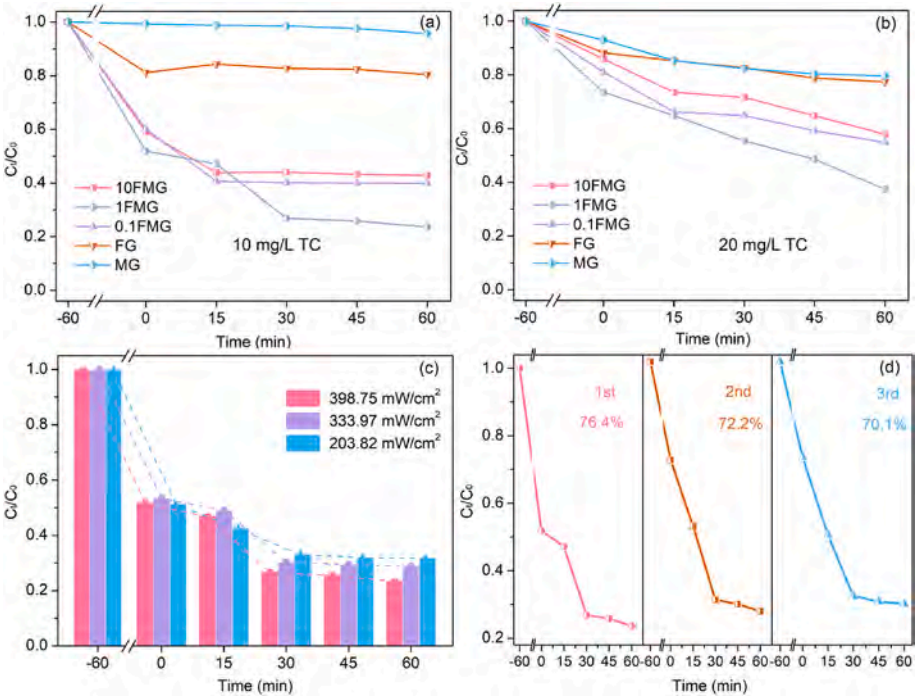

Fig. 5. Degradation efficiency of prepared samples in (a) 10 mg/L TC and (b) 20 mg/L TC; (c) TC degradation over 1FMG under different intensity of light, (d) Cycling runs of 1FMG on TC photodegradation. Conditions: [Catalyst] = 0.2 g/L, [TC] = 10 mg/L.

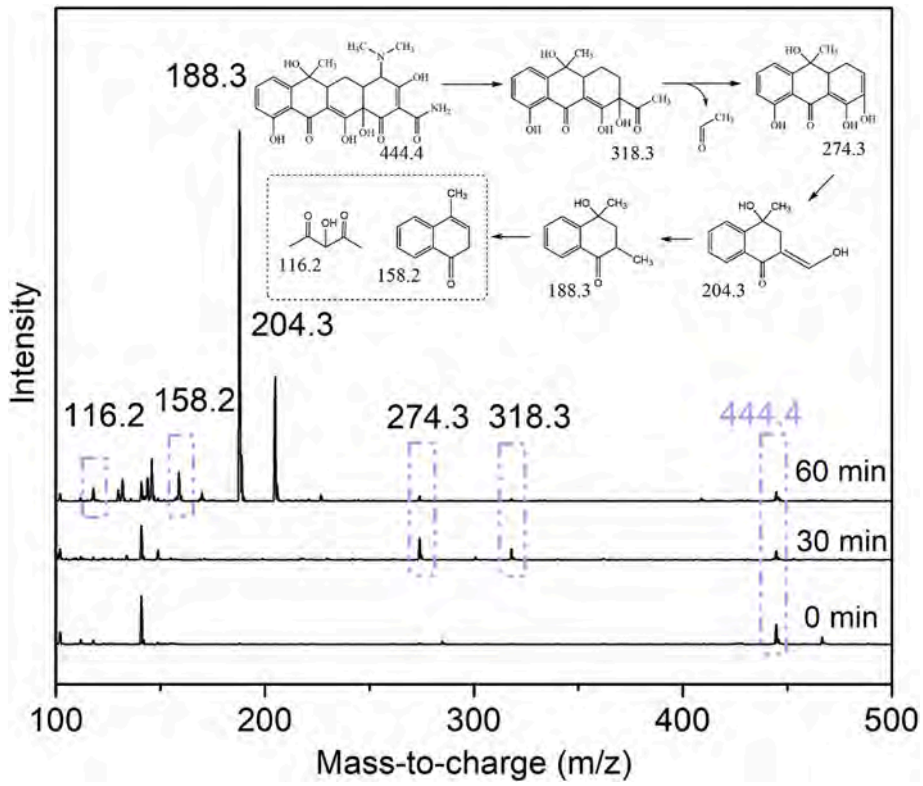

Fig. 6. Degradation intermediates of TC detected by LC-MS. Inset is the possible degradation pathways of TC in the photo-Fenton process over 1FMG.

UV–vis DRS and LSV analysis. According to the DRS in Fig. 4a, all the samples can absorb visible light. LSV curve (Fig. 4b) suggests that all the samples are conductive. Compared with 1FMG, 10FMG and 0.1FMG composites show higher conductivity. Additionally, a peak at 0.85 V appears in FG and a peak at 1.23 V appears in MG. Differently, a peak at 1.00 V appears in 10FMG and a peak at 1.04 V appears in 0.1FMG. No peaks are found in 1FMG. This indicates there has been a reaction between $MnFe_2O_4$ and MoS_2 to form FMG composites. M − S analyses of FG and MG are shown in Fig. S3. It can be found that FG is a p-type semiconductor (negative slope in M − S plot) with the value of Fermi level at 2.12 V vs. *vs.* Ag/AgCl. The bottom of FG VB is more positive (~0.2 eV) than Fermi lever. Therefore, VB value of FG can be calculated to be 2.52 V *vs.* NHE, which is close to the VB value (2.94 V) determined by XPS-VB. The M − S plot of MG exhibits positive slop with the value of Fermi level at −0.08 V vs. *vs.* Ag/AgCl. For MG, Fermi level is more positive (~0.2 eV) than the bottom of conduction band (CB). Therefore, based on the calculations, the CB value of MG is −0.08 V *vs.* NHE.

3.2. Catalytic test

TC, a broad-spectrum antibiotic, is widely used in treating bacterial infections for human health. With the increase of daily dosage, TC emissions into water have been rising. The accumulated TC is a potential hazard for beings. TC is chosen as the main target pollutant to test the performance and stability of FMG under visible-light irradiation. The prepared FMG in this work is anticipated to show high catalytic activity. The effects of different mass ratio of $MnFe_2O_4/MoS_2$, TC concentration, and light intensity on catalytic performance are investigated. The stability of catalyst is studied by cycling experiments. The intermediate products in TC degradation process is explored by LC-MS. Before irradiation, 1 h of dark adsorption needs to be carried out to reach absorption equilibrium (Fig. S4).

Fig. 5a shows the degradation efficiency of the prepared samples on 10 mg/L TC. 1FMG shows the best performance with the efficiency located at 76.4 %. 10FMG and 0.1FMG can remove 57.2 % and 60.0 % TC in 1 h, respectively, higher than the degradation efficiency of FG (19.5 %) and MG (4.4 %). This indicating there is a synergism between $MnFe_2O_4$ and MoS_2 in FMG composites for TC degradation. Fig. 1b exhibits the performance of these samples on 20 mg/L TC degradation. The results are consistent with the degradation efficiency on 10 mg/L TC. Compared the results in Fig. 5a and b, it can be found that the concentration of TC has an impact on the degradation efficiency. The lower concentration leads to higher efficiency, which is beneficial for practical TC (like 1.62 mg/L) treatment.

Afterwards, the effect of light intensity is investigated by adjusting the distance between the light source and TC solution surface. The distance is set at 5 cm, 10 cm and 15 cm, corresponding to 398.75 mW/cm^2, 333.97 mW/cm^2 and 203.82 mW/cm^2, and the TC degradation efficiency reaches 76.4 %, 71.2 % and 68.2 %, respectively. With the decrease of light intensity, the efficiency is also reduced. The degradation efficiency is reduced by ~4 % with the decrease of 100 mW/cm^2.

The stability is an important factor as a catalyst. In this work, the stability and reusability of 1FMG are tested by cyclic experiments. As shown in Fig. 5d, the photo-Fenton process over 1FMG can degrade 76.4 % of TC. 1FMG are recycled via magnetic separation. In the second and third run, TC degradation reaches 72.2 % and 70.1 %, respectively. The reduced efficiency might be owing to the reduced adsorption capacity (from 48.1 % to 28.5 % and 27.6 %). After the first use, some TC or intermediates remain in 1FMW and are not been eluted out, shielding part of the active sites and leading to a decrease in degradation efficiency.

The degradation products of TC over 1FMG are detected via HPLC-MS (Fig. 6). The peak at m/z = 444.4 representing TC is decreasing during the reaction process. Peaks located at other m/z positions appear successively after irradiation. The peaks at m/z = 274.3 and 318.3 are decreasing as the reaction time increased. And after 60 min of irradiation, peaks at m/z = 116.2, 158.2, 188.3 and 204.3 appear, indicating the production of smaller molecules. These small molecular products are more biodegradable. Based on the m/z value, the intermediates can be obtained. Possible degradation pathways of TC are presented (Inset in

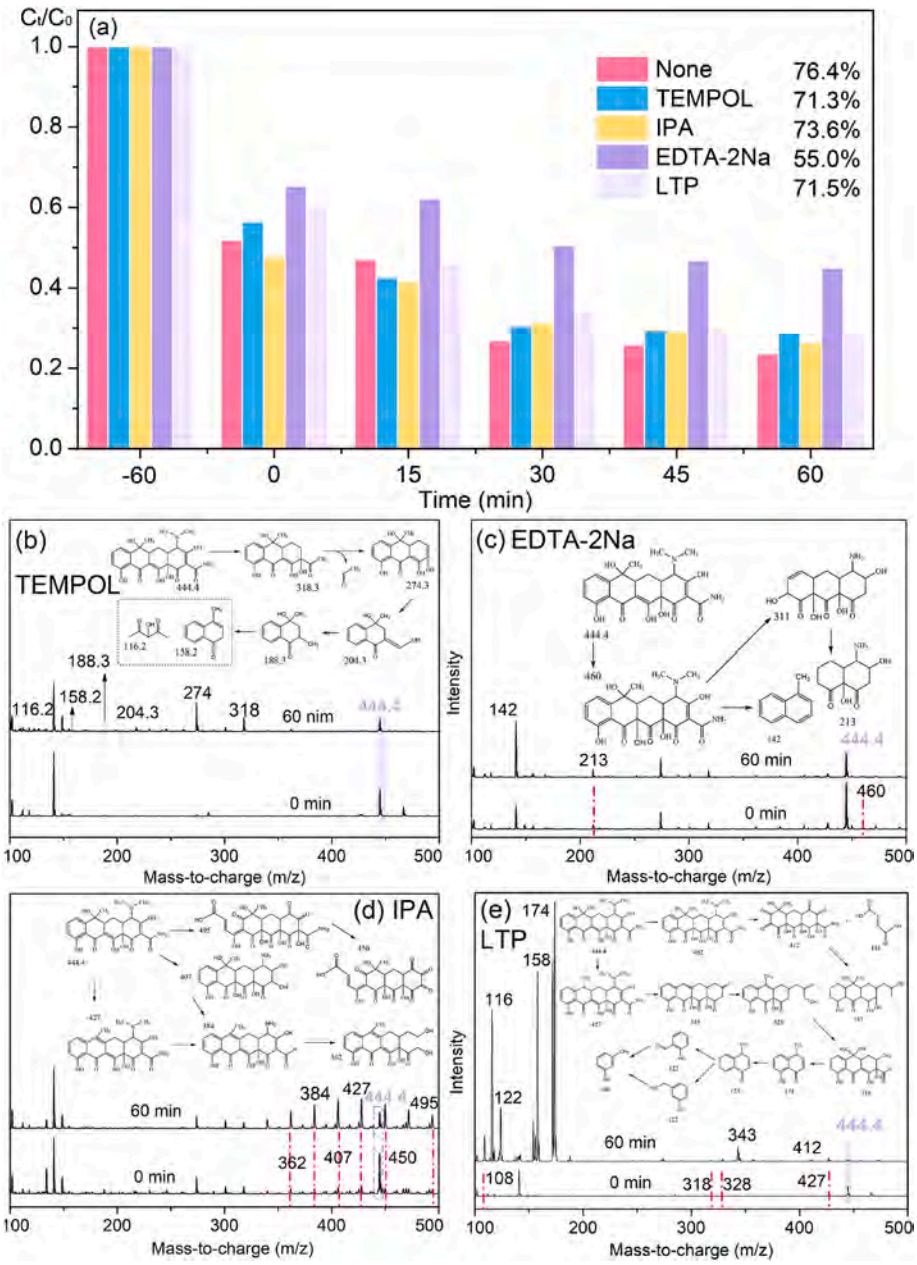

Fig. 7. (a) Trapping tests: 5 mmol scavengers in 100 mL 10 mg/L TC solution; LC-MS spectra and proposed possible TC degradation pathways of the photo-Fenton process after adding (b) TEMPOL, (c) EDTA-2Na, (d) IPA, and (e) LTP.

Fig. 6). There are two main reactions in TC degradation over 1FMG: one is N-demethylation reaction that dominated by h^+, the other one is dehydration/hydroxylation reaction that dominated by •OH (Deng et al., 2018).

3.3. Role of radical species

Trapping tests are used to analyze the role of radical species generated in the photo-Fenton process over 1FMG. TEMPOL, IPA, EDTA-2Na, and LTP are used as the scavengers for $•O_2^-$, •OH, h^+, and $^1O_2$, respectively. As shown in Fig. 7a, after adding the scavengers, all the degradation efficiencies decrease. EDTA-2Na shows the highest inhibit effect with the degradation efficiency reduced to 55.0 %. This suggests that h^+ plays the most important role in TC degradation. Moreover, compared with the degradation efficiency of the process without adding scavengers, 5.1 %, 2.8 % and 4.9 % of the efficiency is reduced after adding TEMPOL, IPA and LTP, respectively. Trapping $•O_2^-$, •OH, and $^1O_2$ has a little negative impact on TC degradation, indicating that $•O_2^-$, •OH, and $^1O_2$ also play a role in the oxidation process.

LC-MS is used to detect the products of trapping test. Degradation results are consistent with that of trapping tests that are determined by UV–Vis spectrophotometer. Possible TC degradation pathways after adding scavengers are also proposed. Fig. 7b shows the LC-MS spectra of the TC degradation intermediates of the photo-Fenton process with adding TEMPOL, which are similar to that of normal photo-Fenton process. The degradation pathway is the same to that in Fig. 6. This suggests that no $•O_2^-$ is generated in the reaction, but the addition of TEMPOL as an organic leads to a competition with TC, so having a little effect on LC-MS spectra. Besides, we also found that compared the LC-MS spectrum in 0 min with that after 60 min of reaction, most TC is not be removed after adding EDTA-2Na (Fig. 7c). And notably, it can be found that nearly no small molecules ($m/z < 360$) are produced after adding IPA (Fig. 7d), while smaller products ($m/z < 200$) can be detected after adding LTP (Fig. 7e). Aromatic ring and naphthol ring

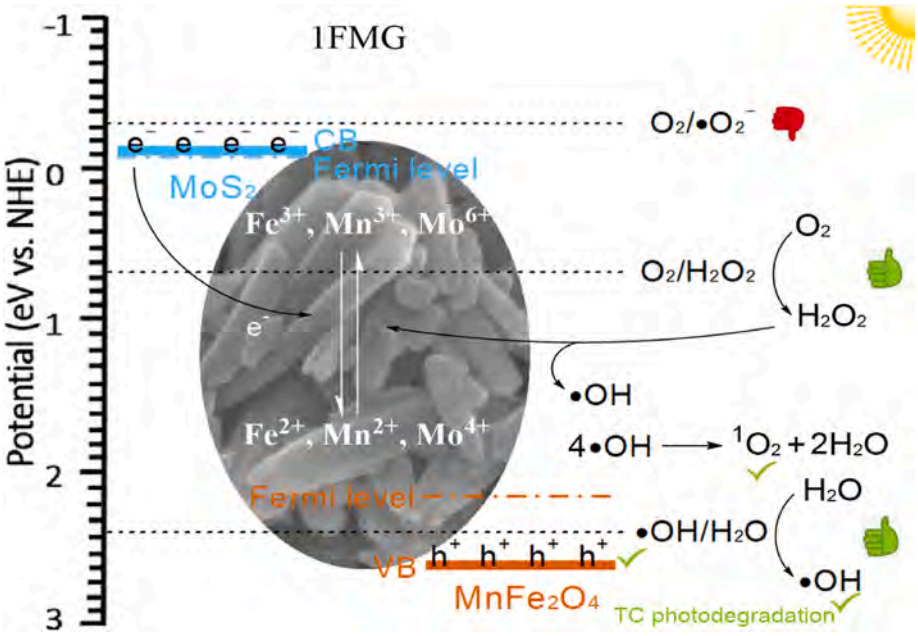

Fig. 8. Possible oxidation mechanisms over 1FMG composite.

were hardly to be broken when IPA was added to trap •OH, affecting the mineralization process. And TOC removal of the TC solution with adding TEMPOL, IPA, EDTA-2Na, and LTP was about 57 %, 28 %, 33 % and 60 %, respectively. It could be concluded that: i) h^+ plays a key role in TC removal, ii) •OH has a great impact on the mineralization ability of the photo-Fenton process.

3.4. Mechanism study

1FMG composite shows much higher degradation efficiency (76.4 %) than that of FG (19.5 %) and MG (14. %), indicating there is a synergism between $MnFe_2O_4$ and MoS_2 in FMG composites for TC degradation. The presence of Fe^{3+}/Fe^{2+}, Mn^{3+}/Mn^{2+} and Mo^{6+}/Mo^{4+} plays an important role in the synergism. The reaction rate of Fe^{3+}/Mn^{3+} and Fe^{2+}/Mn^{2+} cycles is limited owing to the low electron transfer rate in the photo-Fenton process over $MnFe_2O_4$. The introduction of MoS_2 promotes the electron cycle and ensures the enough presence of metal ions with lower valence state (i.e., Fe^{2+}, Mn^{2+} and Mo^{4+}) for H_2O_2 decomposition. Therefore, the photo-Fenton reaction efficiency can be guaranteed. On the basis of above results, h^+, •OH, and $^1O_2$ are generated in the photo-Fenton process of 1FMG, and then participate in the TC degradation. The main active species, h^+, is generated in 1FMG VB after irradiation. The conversion of Fe^{2+}/Fe^{3+}, Mn^{2+}/Mn^{3+}, and Mo^{4+}/Mo^{6+} benefit the separation of photogenerated electrons and h^+. No $\bullet O_2^-$ is produced in the photo-Fenton process. The value of CB (−0.08 V *vs. NHE*) is more positive than the redox potential needed for $\bullet O_2^-$ generation ($E(O_2/\bullet O_2^-)$ = −0.33 V *vs. NHE*), confirming that $\bullet O_2^-$ cannot be produced. •OH can be generated from the oxidation reaction of H_2O owing to the higher VB value than the redox potential of $\bullet OH/H_2O$ (+2.38 V). $^1O_2$ can be generated from the oxygen activation or the disproportionation reaction of •OH. The mechanism of the active species generation in the photo-Fenton process over 1FMG and their roles in TC degradation are presented in Fig. 8.

4. Conclusion

Overall, among these FMG composites, 1FMG are successfully synthesized according to the detailed analysis on its component, structure, morphology and property. The conductive stick-like 1FMG (~2 × 0.3 μm) composites are well dispersed and not accumulated. Fe^{2+}, Fe^{3+}, Mn^{2+}, and Mn^{3+} co-exist in IFMG, benefiting the electrons transfer. Compared with other samples, 1FMG shows the best performance for TC degradation with the removal efficiency reaches 76.4 %. Lower TC concentration leads to higher efficiency, which is beneficial for practical TC (almost <10 mg/L) treatment. Light intensity exhibits positive correlation with the catalytic activity. Active species include h^+, •OH and $^1O_2$ participate in TC photodegradation. Although •OH has a little impact on TC removal, it act as a key role in the mineralization of TC. The excellent catalytic performance can be attributed to following reasons: (i) the presence of metal ions with variable valence state can improve the separation of photogenerated electrons and h^+, guaranteeing the enough generation of h^+. (ii) h^+ plays the main role in TC degradation. (iii) $^1O_2$ possessing high oxidation ability is also formed in the photo-Fenton process over 1FMG. (iv) •OH promotes the mineralization of TC. Particularly, the photo-Fenton process over 1FMG shows great potentials in the applications of antibiotics treatment.

Credit author statement

Huan Yi: Providing inspirational idea; Writing – original draft. Cui Lai: Investigation; providing visionary thoughts. Eydhah Almatrafi: Conception of the study; Writing – original draft. Xiuqin Huo: Design and execution of all the experiments. Lei Qin: Execution of degradation experiments. Yukui Fu: Acquisition and analysis of data. Chenyun Zhou: Interpretation the intellectual content of the paper; Writing – review & editing Zhuotong Zeng: Critical revision of the intellectual content of the paper; Supervision; Project administration. Guangming Zeng: Providing visionary thoughts; review & editing; Supervision; Funding acquisition.

Declaration of competing interest

The authors declare that they have no known competing financial interests or personal relationships that could have appeared to influence the work reported in this paper.

Acknowledgements

This study was financially supported by the Program for the National Natural Science Foundation of China (U20A20323, 51521006, 51879101, 51579098, 51779090, 52100183), the National Program for

Support of Top–Notch Young Professionals of China (2014), the Science and Technology Innovation Program of Hunan Province (2021RC2057), the Hunan Provincial Innovation Foundation for Postgraduate (CX20190260), Hunan Natural Science Foundation (2020JJ3009), Hunan Researcher Award Program (2020RC3025), and the Fundamental Research Funds for the Central Universities (531119200086, 531118010114, 531118040083, 541109060031, 531118010473), and the National Natural Science Foundation of Changsha (kq2007059).

Appendix A. Supplementary data

Supplementary data to this article can be found online at https://doi.org/10.1016/j.chemosphere.2021.132494.

References

Chen, J., Wen, W., Kong, L., Tian, S., Ding, F., Xiong, Y., 2014. Magnetically separable and durable MnFe2O4 for efficient catalytic ozonation of organic pollutants. Ind. Eng. Chem. Res. 53, 6297–6306.

Chen, L.-Y., Xu, F.-F., Zhang, J., Ding, H., Yang, J., 2020. Structure design of CeO2–MoS2 composites and their efficient activity for imine synthesis. Appl. Nanosci. 10, 233–241.

Deng, Y., Tang, L., Zeng, G., Wang, J., Zhou, Y., Wang, J., Tang, J., Wang, L., Feng, C., 2018. Facile fabrication of mediator-free Z-scheme photocatalyst of phosphorous-doped ultrathin graphitic carbon nitride nanosheets and bismuth vanadate composites with enhanced tetracycline degradation under visible light. J. Colloid Interface Sci. 509, 219–234.

Fu, Y.K., Zeng, G.M., Lai, C., Huang, D.L., Qin, L., Yi, H., Liu, X.G., Zhang, M.M., Li, B.S., Liu, S.Y., Li, L., Li, M.F., Wang, W.J., Zhang, Y.J., Pi, Z.J., 2020. Hybrid architectures based on noble metals and carbon-based dots nanomaterials: a review of recent progress in synthesis and applications. Chem. Eng. J. 399, 125743 https://doi.org/10.1016/j.cej.2020.125743.

Gautam, S., Shandilya, P., Priya, B., Singh, V.P., Raizada, P., Rai, R., Valente, M.A., Singh, P., 2017. Superparamagnetic MnFe2O4 dispersed over graphitic carbon sand composite and bentonite as magnetically recoverable photocatalyst for antibiotic mineralization. Separ. Purif. Technol. 172, 498–511.

Hou, S., Mahadevegowda, S.H., Lu, D.R., Zhang, K.X., Chan-Park, M.B., Duan, H.W., 2021. Metabolic labeling mediated targeting and thermal killing of gram-positive bacteria by self-reporting Janus magnetic nanoparticles. Small 17, 2006357.

Li, B.S., Lai, C., Zhang, M.M., Zeng, G.M., Liu, S.Y., Huang, D.L., Qin, L., Liu, X.G., Yi, H., Xu, F.H., An, N., Chen, L., 2020a. Graphdiyne: a rising star of electrocatalyst Support for energy conversion. Adv. Energy Mater. 10.

Li, L., Liu, S., Cheng, M., Lai, C., Zeng, G., Qin, L., Liu, X., Li, B., Zhang, W., Yi, Y., Zhang, M., Fu, Y., Li, M., Long, M., 2020b. Improving the Fenton-like catalytic performance of MnOx-Fe3O4/biochar using reducing agents: a comparative study. J. Hazard. Mater., 124333

Liu, X., Huang, D., Lai, C., Zeng, G., Qin, L., Wang, H., Yi, H., Li, B., Liu, S., Zhang, M., Deng, R., Fu, Y., Li, L., Xue, W., Chen, S., 2019. Recent advances in covalent organic frameworks (COFs) as a smart sensing material. Chem. Soc. Rev. 48, 5266–5302.

O'Neill, J., 2016. Tackling drug-resistant infections globally: final report and recommendations. Rev. Antimicrobial Resist. Government of the United Kingdom https://amr-review.org/sites/default/files/160525_Final_paper_with_cover.pdf. (Accessed 16 April 2021).

Pang, Y., Kong, L., Chen, D., Yuvaraja, G., 2019. Rapid Cr(VI) reduction in aqueous solution using a novel microwave-based treatment with MoS_2-$MnFe_2O_4$ composite. Appl. Surf. Sci. 471, 408–416. https://doi.org/10.1016/j.apsusc.2018.11.180.

Samakchi, S., Chaibakhsh, N., Moradi-Shoeili, Z., 2018. Synthesis of MoS_2/$MnFe_2O_4$ nanocomposite with highly efficient catalytic performance in visible light photo-Fenton-like process. J. Photochem. Photobiol. Chem. 367, 420–428.

Shao, S.C., Wu, X.W., 2020. Microbial degradation of tetracycline in the aquatic environment: a review. Crit. Rev. Biotechnol. 40, 1010–1018.

Shen, Y., Wang, L., Wu, Y., Li, X., Zhao, Q., Hou, Y., Teng, W., 2015. Facile solvothermal synthesis of $MnFe_2O_4$ hollow nanospheres and their photocatalytic degradation of benzene investigated by in situ FTIR. Catal. Commun. 68, 11–14.

Stokes, J.M., Yang, K., Swanson, K., Jin, W.G., Cubillos-Ruiz, A., Donghia, N.M., MacNair, C.R., French, S., Carfrae, L.A., Bloom-Ackerman, Z., Tran, V.M., Chiappino-Pepe, A., Badran, A.H., Andrews, I.W., Chory, E.J., Church, G.M., Brown, E.D., Jaakkola, T.S., Barzilay, R., Collins, J.J., 2020. A deep learning approach to antibiotic discovery. Cell 180, 688.

Vesel, A., Zaplotnik, R., Gaillard, N., 2018. Synthesis of MoS_2 by treating molybdenum in H_2S plasma. Materiali in Tehnologije 52, 417–421.

Wang, X., Wang, A., Ma, J., 2017. Visible-light-driven photocatalytic removal of antibiotics by newly designed C_3N_4@$MnFe_2O_4$-graphene nanocomposites. J. Hazard. Mater. 336, 81–92.

Wang, Z., Lai, C., Qin, L., Fu, Y., He, J., Huang, D., Li, B., Zhang, M., Liu, S., Li, L., Zhang, W., Yi, H., Liu, X., Zhou, X., 2020. ZIF-8-modified $MnFe_2O_4$ with high crystallinity and superior photo-Fenton catalytic activity by Zn-O-Fe structure for TC degradation. Chem. Eng. J. 392, 124851 https://doi.org/10.1016/j.cej.2020.124851.

Yang, S.S., Huang, Z.Y., Wu, P.X., Li, Y.H., Dong, X.B., Li, C.Q., Zhu, N.Y., Duan, X.D., Dionysiou, D.D., 2020. Rapid removal of tetrabromobisphenol A by alpha-Fe_2O_{3-x}@Graphene@Montmorillonite catalyst with oxygen vacancies through peroxymonosulfate activation: role of halogen and alpha-hydroxyalkyl radicals. Appl. Catal. B Environ. 260, 118129 https://doi.org/10.1016/j.apcatb.2019.118129.

Yang, Y., Zeng, Z., Zhang, C., Huang, D., Zeng, G., Xiao, R., Lai, C., Zhou, C., Guo, H., Xue, W., Cheng, M., Wang, W., Wang, J., 2018. Construction of iodine vacancy-rich BiOI/Ag@AgI Z-scheme heterojunction photocatalysts for visible-light-driven tetracycline degradation: transformation pathways and mechanism insight. Chem. Eng. J. 349, 808–821.

Yi, H., Jiang, M., Huang, D.L., Zeng, G.M., Lai, C., Qin, L., Zhou, C.Y., Li, B.S., Liu, X.G., Cheng, M., Xue, W.J., Xu, P., 2018. Advanced photocatalytic Fenton-like process over biomimetic hemin-Bi_2WO_6 with enhanced pH. J. Taiwan Inst. Chem. Eng. 93, 184–192.

Yi, H., Yan, M., Huang, D.L., Zeng, G.M., Lai, C., Li, M.F., Huo, X.Q., Qin, L., Liu, S.Y., Liu, X.G., Li, B.S., Wang, H., Shen, M.C., Fu, Y.K., Guo, X.Y., 2019. Synergistic effect of artificial enzyme and 2D nano-structured Bi_2WO_6 for eco-friendly and efficient biomimetic photocatalysis. Appl. Catal. B Environ. 250, 52–62.

Yu, Z., Rabiee, H., Guo, J., 2021a. Synergistic effect of sulfidated nano zerovalent iron and persulfate on inactivating antibiotic resistant bacteria and antibiotic resistance genes. Water Res. 198, 117141.

Yu, Z., Wang, Y., Henderson, I.R., Guo, J., 2021b. Artificial sweeteners stimulate horizontal transfer of extracellular antibiotic resistance genes through natural transformation. ISME J. https://doi.org/10.1038/s41396-021-01095-6.

Yu, Z., Wang, Y., Lu, J., Bond, P.L., Guo, J., 2021c. Nonnutritive sweeteners can promote the dissemination of antibiotic resistance through conjugative gene transfer. ISME J. 15, 2117–2130.

Zhang, X.-J., Wang, G.-S., Cao, W.-Q., Wei, Y.-Z., Liang, J.-F., Guo, L., Cao, M.-S., 2014. Enhanced microwave absorption property of reduced graphene oxide (RGO)-$MnFe_2O_4$ nanocomposites and polyvinylidene fluoride. ACS Appl. Mater. Interfaces 6, 7471–7478.

Zhao, W., Wei, Z., Zhang, X., Ding, M., Huang, S., Yang, S., 2020. Magnetic recyclable $MnFe_2O_4$/CeO_2/SnS_2 ternary nano-photocatalyst for photo-Fenton degradation. Appl. Catal., A 593, 117443. https://doi.org/10.1016/j.apcata.2020.117443.

Zhong, Y., Shih, K., Diao, Z., Song, G., Su, M., Hou, L.a., Chen, D., Kong, L., 2021. Peroxymonosulfate activation through LED-induced $ZnFe_2O_4$ for levofloxacin degradation. Chem. Eng. J. 417, 129225. https://doi.org/10.1016/j.cej.2021.129225.